Available online at www.sciencedirect.com

ScienceDirect

Advances in Space Research 55 (2015) 2166–2176

ADVANCES IN SPACE RESEARCH (a COSPAR publication)

www.elsevier.com/locate/asr

Radio reflection imaging of asteroid and comet interiors II: Results and recommendations

Robert E. Grimm [a,*], David E. Stillman [a], Paul Sava [b], Detchai Ittharat [b]

[a] Planetary Science Directorate, Southwest Research Institute, 1050 Walnut St. #300, Boulder, CO 80302, USA
[b] Center for Wave Phenomena, Colorado School of Mines, 1500 Illinois Street, Golden, CO 80401, USA

Received 3 July 2014; received in revised form 13 January 2015; accepted 29 January 2015
Available online 7 February 2015

Abstract

We modeled orbital surface-penetrating radar of an asteroid and comet using two-dimensional finite-difference wavefield migration, in order to assess key target properties and experiment parameters required to fully image internal structure. Migration places radar echoes in their correct positions in a complex subsurface and is a complementary tool to travel-time tomography. The target shape was scaled from 433 Eros to 0.5-km mean diameter for an asteroid and 10 km for a comet. The interiors were populated with a power-law distribution of spherical blocks. We used an image structural similarity index to compare the internal surfaces reconstructed under different assumptions to a "best" image using optimum parameters. We found that successful internal imaging of the asteroid was not sensitive to whether the block interstices were regolith or void. Frequency dependence between 5 and 15 MHz was also minor. Internal interfaces could also be imaged if the attenuation was higher than that inferred within volcanic plains on Mars, but not as high as measured in a strongly fractured volcanic tuff on Earth. The overall imaging quality for the comet was statistically similar to the asteroid, but there was less variability due to smaller internal contrasts. A key finding is that imaging was vastly improved by using a second spacecraft as a radar receiver. A subsatellite with a different orbit will eventually provide a range of different illumination geometries over each part of the target. Finally, the results depend strongly on the specified internal velocity distribution, representing partial progress in complementary tomographic velocity estimation. The modeled impedance contrasts within the asteroid are larger than those typically encountered in exploration seismology and very much larger than in medical imaging, and so the velocity used to migrate the reflections must be close to the actual distribution. This again emphasizes the need for joint traveltime tomography and wavefield migration for asteroid imaging, which is optimized using two orbiters.

Keywords: Asteroid; Comet; Surface-penetrating radar

1. Introduction

Asteroids and comets are widely regarded as holding keys to the composition and early dynamical, collisional, and thermal evolution of the Solar System (e.g. Bottke et al. (2002), Festou et al. (2004)). Near-Earth Objects (NEOs) are of particular interest because of the hazards they pose to Earth (e.g. Chapman (2004)) and because they are accessible to exploration. Since 2010, NASA has described NEOs as likely targets for human exploration, and more recently has adopted a robotic Asteroid Retrieval Mission (ARM) to capture a very small (<10-m) object (Brophy et al., 2012).

In addition to understanding their surfaces from remote sensing, the interiors of asteroids and comets are also of interest because they hold records that may span accretion, metamorphism, differentiation, impacts, disruption, and reassembly, perhaps all in tandem with a complex dynamical history. Interior imaging may reveal which bodies

* Corresponding author. Tel.: +1 720 240 0149.
E-mail address: grimm@boulder.swri.edu (R.E. Grimm).

http://dx.doi.org/10.1016/j.asr.2015.01.038
0273-1177/

preserve primordial accretional structure, which show the onset of "planetary" processes such as metamorphism or differentiation, and elucidate how the structure-strength feedback loop produced by collisional evolution is manifested (Binzel et al., 2003).

A close-orbiting spacecraft might measure higher-order terms in the gravity field and infer some crude heterogeneity in the target (Hilton, 2002). Magnetometry will also have poor resolution, and sufficient contrasts in permeability are less certain than those in density. Electromagnetic (EM) induction sounding is unlikely to work because high frequencies (>10 kHz) are necessary to resolve the interiors of small, resistive bodies, but in this regime signals would be propagative (radar-like) and not inductive.

Wavefield methods provide the highest resolution in geophysics. Radar and seismology are closely related approaches to subsurface wavefield imaging, and waves may propagate completely through small bodies. Seismology has been under continuous development for oil and gas exploration since the 1920s (e.g. Sheriff and Geldart (1995)), and ground-penetrating radar (GPR) is rapidly adopting seismic acquisition and processing methods (e.g. Daniels (2004)). Although some preliminary concepts for small-body seismic investigations have been proposed (Huebner and Greenberg, 2001; Walker et al., 2006), here we treat only radiowave (radar) exploration due to its relative simplicity of established noncontacting operation.

Safaeinili et al. (2002) presented an overview of "radio reflection tomography" (RRT) of asteroids and comets, including data collection scenarios, data processing and inversion, and instrumentation implementation. Asphaug et al. (2003, 2010) described possible mission scenarios. The Rosetta Comet Nucleus Sounding Experiment by Radiowave Transmission (CONSERT: Kofman et al., 2007) attempted the first internal imaging of a comet, 67P/Churyumov–Gerasimenko (~4 km diameter). CONSERT is a transmission travel-time tomography experiment (see nomenclature below) with multiple sources (the moving orbiter) and a single receiver (the fixed lander). Without crossing raypaths, true imaging is minimal: the team has suggested that imaging diversity can be improved using multiple internal reflections from the free surface (Barriot et al., 1999; Benna et al., 2004), if sufficient signal-to-noise ratio (SNR) is available. Results are not available at the time of this writing; nonetheless, as the first experiment of its kind, CONSERT can probably be relied on to measure the overall dielectric constant of the target comet—and hence constrain the porosity and ice/rock ratio—and determine if there are any major internal contrasts.

Our objective is to provide guidance for the design of missions for radar imaging of the interiors of comets and small asteroids. We test different target properties, experiment parameters, and knowledge of the velocity model using full-wavefield imaging and we use quantitative metrics to describe how well target structure is recovered. A companion paper (Sava et al., 2015; hereafter Paper I) describes the theory, and this paper gives the results and recommendations.

2. Scope

We seek to define radio transmission or reflection investigations that may be feasible within the present Discovery and proposed Exploration Robotic Precursor Mission (xPRM) Programs (several hundred million dollar lifecycle cost). These surveys can be expressed most simply as the number of sources and receivers and their geometry. Because of the standoff capability of radar, we consider only orbital platforms without surface assets (in contrast to the geometry for the in-progress Rosetta mission).

We adopt the nomenclature and computational methods of exploration seismology (e.g. Sheriff and Geldart (1995)), by far the most highly developed suite of geophysics due to its importance in oil and gas exploration. *Imaging* refers to all methods that produce a "picture" of the interior of a body. There are two major branches of geophysical imaging: tomography and migration. *Tomography*, literally "slicing," can also be described as *volume* imaging and generally produces a continuum of material properties. Tomography can use simple ray methods although it is more accurate, especially where large velocity contrasts exist, when using first arrivals from wavefield calculations. *Migration* uses wavefield calculations to reposition reflections to their true locations (Claerbout, 1985; Yilmaz, 2001; Bondi, 2006; see also Paper I). Therefore it is sensitive to sharp material contrasts and can be described as internal *surface* imaging.

Tomography and migration are complementary: tomography typically uses direct, through-going rays and hence large source-receiver separations ("apertures"), whereas smaller apertures capture the reflections used for migration. For asteroids and comets, however, these considerations might be changed: if the farside surface reflection can be detected, tomography can also exploit a small aperture, and we argue here and in Paper I for larger migration apertures. *Migration tomography* iteratively combines both methods: a velocity model is tomographically improved and passed to the migration analysis, which updates the positions of interfaces for the next tomography pass. Migration tomography is computationally expensive and is generally reserved for regions of complex structure. *Full-waveform imaging* is the state of the art and most computationally intense, wherein the entire wave train is iteratively matched to a model prediction.

We investigate only migration in this preliminary study, using several a priori velocity models to simulate the effect of progressive tomographic improvements. Data from an actual asteroid or comet mission in the 2020s or beyond will likely use migration tomography or full-waveform imaging. We further restrict the study to two-dimensional

(2D) targets derived from a three-dimensional (3D) model. We assess all imaging results using quantitative metrics.

3. Model and methods

3.1. Target bodies

We adopted the three-dimensional digital shape model of asteroid 433 Eros (Gaskell, 2008) as a representative external geometry for both asteroids and comets. Its irregular "potato" shape is not extreme, but is sufficiently far from spherical to provide more realistic tests of imaging algorithms. The best-fitting triaxial ellipsoid to Eros has dimensions of $34.4 \times 11.2 \times 11.2$ km. We scaled this shape to mean dimensions of $1 \times 0.33 \times 0.33$ km to represent a small Near-Earth Asteroid (NEA) and to $21 \times 7 \times 7$ km to represent a comet. The 0.5-km mean diameter of the model asteroid is close to that of the OSIRIS-Rex mission target, 101955 Bennu (Nolan et al., 2013), whereas the comet's 10-km mean diameter is comparable to 1P/Halley and 10P/Tempel 2.

3.1.1. Structural models

We treated the interiors of both asteroids and comets as rubble piles (Richardson et al., 2002; Weissman et al., 2004): recognizing an object as monolithic rock or ice, or a uniform "sandpile" of fine-grained material would be scientifically important but uninteresting from the perspective of an imaging study. Conversely, objects that are shattered (massively fractured but with blocks preserved in situ: Richardson et al., 2002) would be more challenging to image due to subwavelength crack thicknesses, and are deferred to a later study. For rubble piles and shattered objects, the size-frequency distribution (SFD) of internal blocks—in particular, the size of the largest block—provides insights on collisional history (Leinhardt et al., 2000; Michel et al., 2004, and references therein; Durda et al., 2007).

We populated the interior of the irregularly shaped 3D model asteroid with spherical blocks using the geometric algorithm of Tanga et al. (1999). The size of the largest block is specified and randomly placed tangentially to the object's surface. We relaxed this constraint to cut the first spherical block and place that plane tangent to the surface. Then a location is randomly picked and the largest possible block that does not overlie the first block is inscribed. In practice, some overlap may be allowed. This algorithm is followed until all voids down to some minimum size or maximum number of blocks is reached. The results also depend on the number of surface vertices selected in the shape model. We carried out a number of random trials, varying the number of surface vertices, the size of the largest block, the number of blocks, and the allowed block overlap. We selected one realization with 30 surface vertices, 200-m largest block, 300 blocks, and no overlap. Fig. 1 shows the full 3D model and the slice selected for 2D radar modeling.

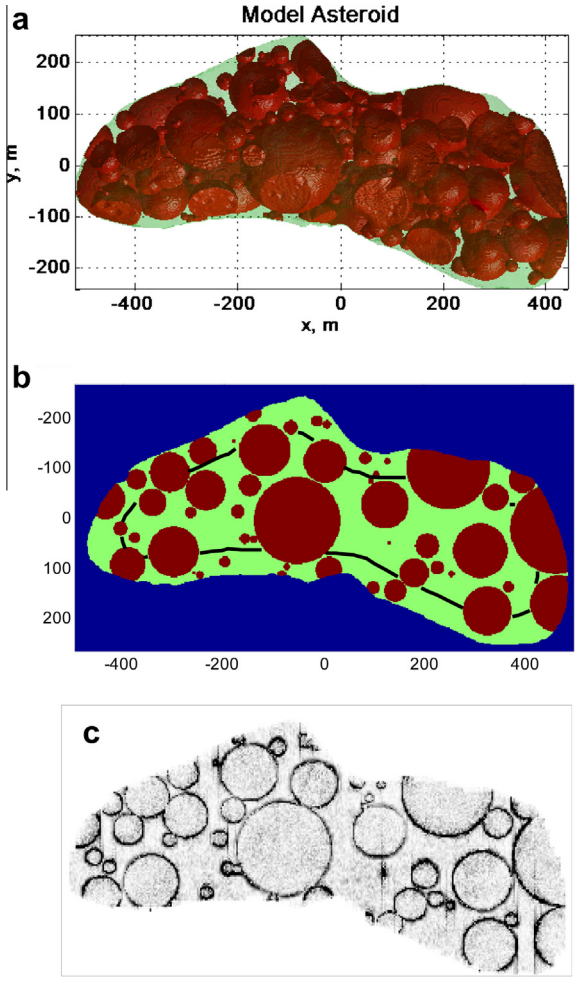

Fig. 1. Model target geometry and optimum wavefield-imaging reconstruction. (a) The shape of asteroid 433 Eros was scaled to a mean diameter of approximately 500 m and populated with non-overlapping spheres with maximum diameter 200 m. The spheres (red) are considered "rock" and the interstitial material (green) is "regolith." The same model and interior structure was scaled to a mean diameter of 10 km to simulate a comet, with adjustments to material properties for "rock" vs "regolith." An alternative "void" model for the asteroid treats all regolith below 50-m depth (black line in b) as free space. (b) Slice in xy plane ($z = 0$) for 2D modeling. (c) Best 2D reconstruction of regolith interior model using lossless media and large aperture at 15 MHz. The image shows the (unipolar) envelope of the analytic signal of the wavefield reconstruction and has been both spatially renormalized and stretched. The vertical lines are minor artifacts of the analytic signal calculation that are present in all of the reconstructions. The surface reflection has been masked out so it does not contribute to quantitative comparisons of this Best reconstruction with others.

The SFD for this realization varies approximately as the –3 power and the largest block is 13% of the population mass. The observed NEA population and the results of collisional simulations have power-law slopes -1 to -4 depending on the study and size range (Werner et al., 2002; Stuart and Binzel, 2004; Durda et al., 2007), whereas the mass of the largest fragment varies from ~ 1 to $<10^{-3}$ with increasing specific impact energy (Durda et al., 2007). Thus we make no particular claim about what our

geometric construction may imply physically; we simply note that it is physically plausible.

The selected asteroid model is comprised of approximately 50% blocks and 50% regolith by volume. For an asteroid bulk density 2 Mg/m^3 (approximately the mean of S and C types; Carry, 2012), appropriate block and regolith densities might be 3 and 1 Mg/m^3, respectively. If in turn the block porosity is 10% (typical of meteorites, Britt et al. (2002)), the grain density of the blocks is 3.3 Mg/m^3 and, adopting the same grain density for the regolith, the regolith porosity is 70%. This model does not explicitly include macroporosity as all the block interstices are assumed to be regolith-filled. If, however, the regolith is interpreted as subwavelength porous blocks separated by void, the overall macroporosity is ~33%. This is within the definition of rubble-pile asteroids and both figures are close to the average C-asteroid and somewhat higher than the average (fractured) S-asteroid as reported by Britt et al. (2002). The bulk porosity in any case is 40%.

We wished to investigate an alternative model in which the mean density of the asteroid approached that of Bennu (~1.0 Mg/m^3: Chesley et al. (2012)). However, the minimum density with 50% rocky (3 Mg/m^3) blocks is 1.5 Mg/m^3. Because we assigned higher priority to maintaining the same material properties, we instead specified a transitional model where all regolith below a depth of 50 m was replaced with void (free space). This "void pile" model has mean density of ~1.7 Mg/m^3, bulk porosity 50%, and equivalent macroporosity 44%.

We used the same realization of randomized internal structure for a comet, but scaled to 10-km mean diameter. We assumed the blocks were solid ice and the regolith was ice with 67% porosity, representative of fresh firn (Trudinger et al., 1997). In reality, there may be three phases of H_2O to consider: low-density amorphous (LDA), cubic crystalline (Ic), and cubic hexagonal (Ih) (see Petrenko and Whitworth (1999), for a review), plus differences in consolidation.

3.1.2. Electromagnetic wave velocities

The speed of light v in a medium with dielectric constant (relative permittivity) ε is $v = c/\sqrt{\varepsilon}$, where c_0 is the speed of light in vacuum. For dry silicates, $\varepsilon = 1.93^{\rho}$, where ρ is the bulk density (Olhoeft and Strangway, 1973). Therefore $v = 0.11$ and 0.22 m/ns for the rock and regolith portions of the model asteroid, respectively. For solid ice, $v = 0.17$ m/ns using $\varepsilon = 3.15$ (Petrenko and Whitworth, 1999), whereas the comet "regolith" $v = 0.24$ m/ns was derived assuming an exponent 2.7 (percolation-threshold) power-law mixing model for ice (Stillman et al., 2010). These figures are repeated in Table 1 for convenience.

Table 1
EM wave velocity (m/ns).

Target	Solid	Regolith
Asteroid	0.11	0.22
Comet	0.17	0.24

Void/free space is 0.3 m/ns.

It is worth noting that the derived velocity contrast is 100% between asteroid rubble blocks and regolith, and 40% between the comparable comet structures. Terrestrial seismic exploration for oil and gas commonly deals with impedance contrasts of 3–70% between different sedimentary rocks (Sheriff and Geldart, 1995), whereas medical ultrasound imaging of the human body, apart from bone and lung, sees maximum impedance contrasts <30% (Chan and Perlas, 2011). The strong velocity contrasts likely inherent in asteroid and comet rubble piles will be seen herein to adversely affect imaging quality.

3.1.3. Electromagnetic wave attenuation

Radio waves are attenuated by scattering from dielectric contrasts and by intrinsic absorption (e.g. Grimm et al. (2006)). The former redirects energy away from the receiver whereas the latter converts radiofrequency energy to heat. Dielectric contrasts with spatial scales on the order of a wavelength and larger are captured through conventional wave modeling, e.g., the Fresnel reflection coefficient. Structures much smaller than a wavelength as well as intrinsic absorption can be treated together as a simple loss tangent $\tan\delta$. A complementary measure is the characteristic (1/e) skin depth s: $A = A_0 e^{-x/s}$, where A is amplitude and x is distance. The two are related by $\tan\delta = v/\pi f s = \lambda/\pi s$, where f is the frequency and λ is wavelength in the target (e.g. Grimm et al. (2006)).

Heggy et al. (2007) measured $\tan\delta < 0.005$ from 10 to 100 MHz for three ordinary chondrites, smaller than the lowest value selected below for this study. For chondritic asteroids, we therefore assume that absorption can be neglected and that scattering is the dominant loss mechanism. Absorption in ordinary chondrites is likely dominated by interfacial polarizations between free metal (several percent by volume) and enclosing silicates; classical mixing laws (e.g., Maxwell Garnet; see Sihvola (1999)) indicate that metal abundances would have to increase to several tens of percent (e.g., as inferred for M-type asteroids) before strongly affecting the loss.

We assumed two endmembers for $\tan\delta$ in the model asteroid (Table 2). The high-loss limit was derived from 25 to 50 MHz GPR attenuation studies of the Bishop Tuff, a variably welded, strongly fractured series of pyroclastic flows in California (Grimm et al., 2006). The low-loss limit was derived from 20-MHz orbital radar penetration of "young" volcanic flows on Mars (Stillman and Grimm, 2011). We scaled $\tan\delta \propto 1/\sqrt{f}$, which is intermediate between constant loss tangent (appropriate to multiple overlapping dielectric loss mechanisms) and $\tan\delta \propto 1/f$ (appropriate to constant electrical conductivity).

We treated only a single loss rate for comets based on the electrical conductivity of impurity-saturated ice at 200 K (Grimm et al., 2008), which turns out to be about 1/10 of the lowest loss rate used for the asteroid. Therefore

Table 2
Loss tangents and 1/e attenuation lengths (m).

Case	5 MHz	15 MHz	Notes
Ultra Low	0.005 (2400)	0.002 (2400)	Nominal comet 1–10 dB/km (DC conduction loss in Cl-saturated ice at 200 K; (Grimm et al., 2008))
Low	0.04 (270)	0.02 (160)	Nominal loss Mars volcanic plains (Stillman and Grimm, 2011)
Medium	0.12 (90)	0.07 (50)	Geometric mean of low and high
High	0.39 (27)	0.22 (16)	Scattering loss in Bishop Tuff (Grimm et al., 2006)

there is actually a doubling in total attenuation through the comet compared to the asteroid, as the former is 20 times larger than the latter.

3.2. Experiment parameters

3.2.1. Frequency

The main parameter describing a radar system is the center frequency. We adopted 5 and 15 MHz: the former is at the upper limit of the Mars Advanced Radar for Subsurface and Ionosphere Sounding (MARSIS: Picardi et al. (2004)) and the latter is the low end of the bandwidth of the 20-MHz Mars Shallow Subsurface Radar (SHARAD: Seu et al. (2007)). Computational limits prevented us from working at the SHARAD center frequency, but 5 and 15 MHz are frequencies preferred by Safaeinili et al. (2005). Full-wavefield calculations for a 10-km comet at the 90-MHz CONSERT center frequency were clearly beyond our available resources. The finite-difference wavefield calculations (Paper I; see also Yilmaz (2001)) used the Ricker source wavelet ubiquitous in seismology (e.g. Sheriff and Geldart (1995)), which has 3-dB bandwidth approximately equal to the center frequency. This is comparable to GPR but is higher than the bandwidths of MARSIS or SHARAD. Also, we wish to be clear that, if comparing to real radar systems, the finite-difference approach assumes that the center frequency or "carrier" has been restored. MARSIS and SHARAD downsample the data, returning the full bandwidth but with the carrier stripped, thus reducing the data volume. The Nyquist–Shannon sampling theorem assures that these data are sufficient to restore the original waveform by reinserting the carrier frequency.

3.2.2. Geometry

CONSERT measures traveltime between two spacecraft: an orbiter and a lander. This configuration maximizes SNR and, while useful for deriving bulk dielectric properties of the target, is poor for imaging. All other mission concepts to date use a single orbiter and imply that sufficient imaging quality can be obtained from a co-located transmitter (Tx) and receiver (Rx). In exploration seismology, this geometry is called *zero-offset*; in practice, small (constant) offset profiling is restricted to GPR or minimal seismic systems. *Multi-offset* reflection surveys are the rule in seismology and are emerging in GPR, in which signals from one Tx are received at multiple Rx (geophones or antennae) simultaneously. By moving the Tx and Rx array, data can be extracted that illuminate a particular subsurface patch at a variety of incidence angles, improving SNR. This approach revolutionized exploration seismology in the early 1960s. Modern migration processing is able to operate on all of the raw data simultaneously but still exploits this basic principle. Paper I demonstrates these ideas in detail.

Therefore we treated two cases for orbital geometry: single and dual spacecraft (S/C). The latter would most probably consist of a primary S/C Tx/Rx and a single subsatellite Rx. For the purposes of this study, we simply assumed that slightly different semimajor axes would allow the two S/C to sweep out all angles with respect to each other and the target body (see Paper I); this variable viewing geometry between the two platforms obviates the need for multiple Rx. This assumption is trivial for the 2D case examined in this paper; getting proper coverage in 3D requires consideration of the repeat period of the constellation, the orbital planes of the S/C, and the rotational period of the target. In practice, the capability to transmit and receive orthogonal linear polarizations would be desirable to maximize individual Tx–Rx coupling.

Because we are interested here in reflected phases only, for multi-offset imaging we selected all possible Rx positions within $\pm 60°$ of arc from each Tx position. The Tx itself is swept through 360° around the target. Our results are insensitive to the specific choice of semimajor axes as we included as many positions along the orbit as necessary (every 0.5°) to eliminate aliasing, and the migration procedure collapses surface resolution to sub-Fresnel-zone scales (a fraction of a wavelength).

3.2.3. Image reconstruction

After the experimental geometry and target properties are used to create synthetic data, the migration procedure (Claerbout, 1985; Yilmaz, 2001; Bondi, 2006; Paper I) attempts to invert the data to the true positions of reflecting surfaces. Migration essentially treats every point in the record as a source and runs the wavefield backward in time, which in principle repositions all reflecting events at their true position. It can do this perfectly only for infinitesimally dense data, 0–360° Tx–Rx apertures, no attenuation, and perfect a priori knowledge of the velocity structure. Real-world deviations from these assumptions lead to imperfect imaging. Finite frequencies and bandwidths also limit imaging quality. In the context of this exercise lacking random noise, any deviations in the imaging from reality are deterministic.

For simplicity, we used the scalar (acoustic) wave equation with attenuation. The grid size was 1 and 4 m for the asteroid and comet, respectively, corresponding to at least ~8 points per wavelength at center frequencies of 15 MHz for the asteroid and 5 MHz for the comet.

Migration requires a velocity model. We assessed five models, with migration at (i) the (uniform) average velocity of the target, (ii) the velocity of the rock or block component, (iii) the velocity of the regolith component, (iv) a "blurred" version of the true velocity, representing partial progress on joint migration tomography, and (v) the true velocity. The blurred models were constructed by convolving the true velocity with a 15 × 15-pixel boxcar averaging filter (i.e., 15 m for the asteroid and 60 m for the comet).

We formed "Best" reconstructions against which other models could be compared, defined as the zero-attenuation, multi-offset to 60° aperture, true-velocity migration result for a particular target type, interior material, and frequency. For example, Fig. 1c shows the Best model for the asteroid, void interior, 15 MHz. It is necessary to use an actual migration image rather than just the source wavelet convolved with the indexed image (Fig. 1b) because the wavelength is different in the rock and regolith components.

Table 3
Model combinations.

Property	Values
Asteroid	
Structure	R(ubble pile), V(oid with rubble)
Attenuation	L(ow), M(edium), H(igh)
Frequency	5, 15 MHz
Geometry	S(ingle), D(ual) platforms
Velocity	S(olid), R(egolith), A(verage), B(lurred), T(rue)
Comet	
Structure	R
Attenuation	U(ltra low)
Frequency	5
Geometry	S, D
Velocity	S, R, A, B, T

120 asteroid models, 10 comet models.
Naming convention: A.V.M.15.D.B = asteroid, void with rubble, medium atten, 15 MHz, dual spacecraft, blurred velocity model.

4. Results

Table 3 gives the naming convention for the models as functions of target type, interior structure, attenuation, frequency, geometry, and migration velocity. 120 asteroid and 6 comet models were evaluated. Each Tx–Rx combination of traveltime vs. received amplitude is known geophysically as *trace or record* and in radar and ultrasound as an A-scan. All Rx corresponding to each Tx form a 2D *shot record*. For zero-offset (single S/C) geometry this is one trace per shot record, but comprises multiple traces in multi-offset (dual S/C). The gather of all zero-offset shot records is equivalent to a B-scan. The shot records all around the target are the primary data.

We display the reconstructed wavefield as the amplitude of its analytic signal. This transformation traces an envelope around the positive amplitudes of the wavefield, thus eliminating polarity. Therefore the result is maximized on discontinuities, which optimizes the comparison of the image to the physical model. We apply an Automatic Gain Control (AGC) to boost weaker signals in the target's interior and a linear stretch to improve contrast. The AGC normalizes each point in the interior by the average of all points in a 70-m wide boxcar filter around it. This width was chosen empirically to balance the desired amplitude increase in the center vs excessive noisy contrasts. The stretch saturates all pixels above 5% of the minimum (again, because the largest values are generally at the discontinuities). The surface reflection was masked out so that it does not contribute to the correlation analysis below (see Table 4).

Fig. 2 shows selected results for the asteroid-imaging study. Only images using the true or blurred velocity distribution are presented because all of the constant-velocity migrations performed poorly. This is not surprising, as we discussed above how the velocity contrasts are larger than typically encountered in exploration seismology and are much larger than in medical ultrasound. This indicates that the velocity distribution will have to be constructed iteratively and that good images will only come into focus later in the process.

Qualitatively, it is evident that the internal structure is well imaged at low and medium attenuation: recall that high attenuation was derived from heavily fractured volcanic rocks, so comparable small-scale heterogeneity in the asteroid may strongly affect internal imaging. The higher resolution at 15 MHz compared to 5 MHz is apparent, but the former does not penetrate as deeply as the latter. Dual-orbiter (multi-offset) reconstructions are superior to those using a single orbiter (zero-offset). There may be a slight improvement in imaging contrast for void-interior models over those packed with regolith due to the larger velocity contrast.

Visual impressions from the limited number of comet runs at 5 MHz (Fig. 3) agree with comparable asteroid cases. Internal structure is better in the dual-orbiter reconstructions at the true velocity, but is not so marked for the blurred and average velocities. This is likely a consequence of the smaller velocity contrasts in the comet that reduce multipathing.

5. Analysis

We sought quantitative measures of the effects of target type, interior materials, attenuation, frequency, observation geometry, and velocity model on the comparison of the recovered distribution of internal reflectors to the true structure. We denote the reconstructed data as A_d and the Best model as A_m. We tested four different representations of A_d and A_m: the wavefield normalized by its largest value ("MaxNorm"), the analytic-signal envelope normalized by its largest value, the wavefield spatially normalized by the AGC filter described above, and the AGC-normalized analytic-signal amplitude. The last corresponds to the parameters for Figs. 1c, 2, and 3.

We tested two approaches to comparing A_d and A_m. In the first, we simply computed the correlation coefficient r^2:

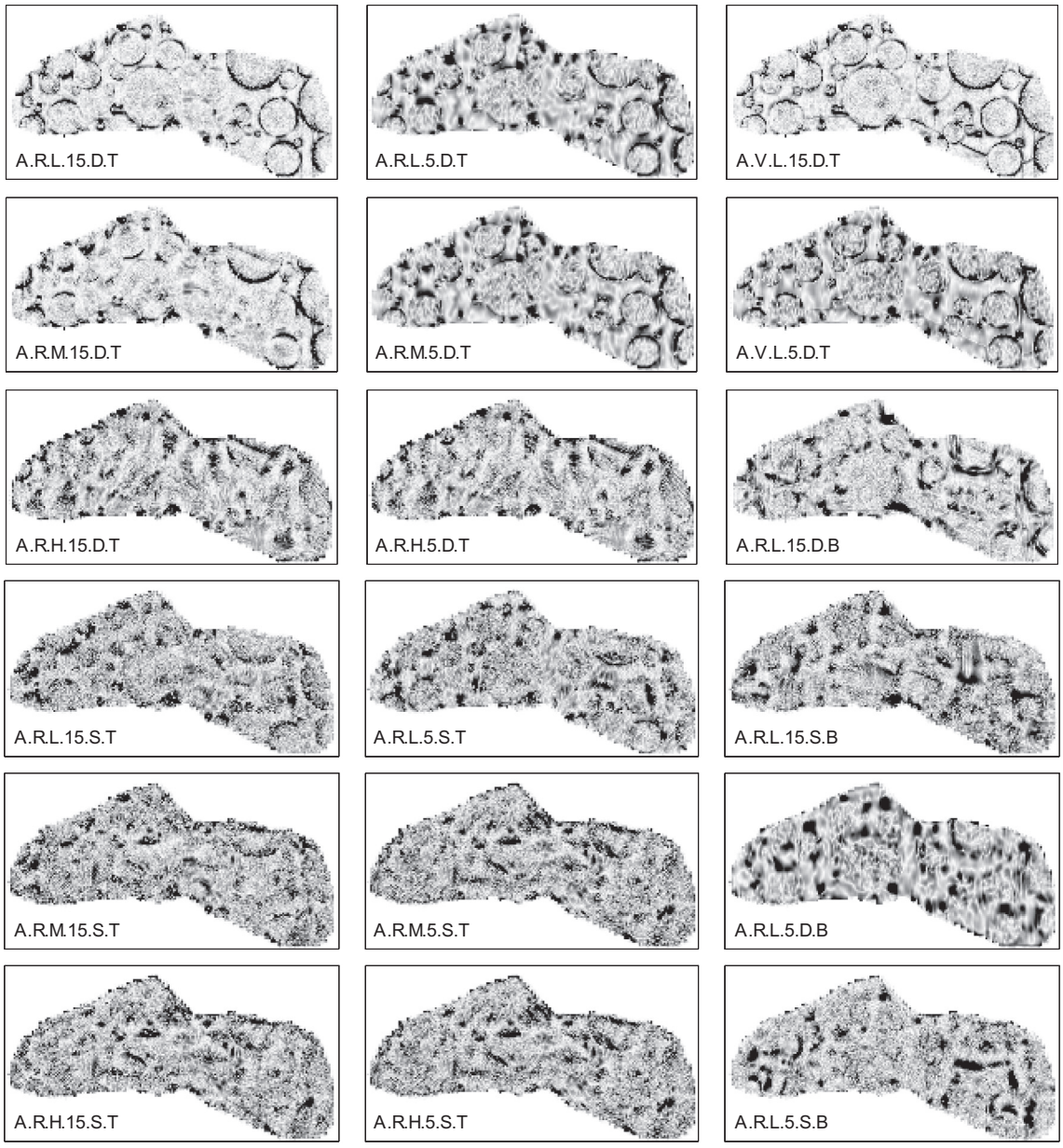

Fig. 2. Selected wavefield-imaging reconstructions of model asteroid structure; see Table 3 for nomenclature. Visually, the best images are formed for low and medium attenuation, lower frequency, dual orbiters, and velocity model close to or at the true distribution. Images using uniform velocities are poor and are not shown.

$$r^2 = 1 - \sum_i \frac{(A_{d,i} - A_{m,i})^2}{(A_{m,i})^2} \tag{1}$$

The correlation coefficient has a maximum value of unity, but can be arbitrarily negative for poor fits. Indeed, we found that r^2 was a poor measure overall for comparison of either the data images or their analytic-signal envelopes, using either normalization. Only the true-velocity reconstructions using the analytic-signal envelope had positive median values. The correlation coefficient is especially sensitive to small-scale noise or mismatches.

We discarded r^2 and used an alternative method developed in the image-processing literature that better represents how image quality is perceived: the structural similarity index (SSIM; Wang et al. (2004)):

$$\mathrm{SSIM} = \frac{(2\mu_m\mu_d + \varepsilon_1)(2\sigma_{md} + \varepsilon_2)}{(\mu_m^2 + \mu_d^2 + \varepsilon_1)(\sigma_m^2 + \sigma_d^2 + \varepsilon_2)} \tag{2}$$

where μ_m and μ_d are the mean values of A_m and A_d, respectively, σ_m and σ_d are the respective standard deviations, σ_{md} is the correlation between the model and data, and ε_1 and ε_2 are small stabilization factors. We found that ε_1 and ε_2 could be made vanishingly small, wherein SSIM reduces to the so-called Universal Quality Index (UQI). SSIM is intended to balance contributions of luminance (μ_m, μ_d), contrast (σ_m, σ_d), and structure (σ_{md}) on how the

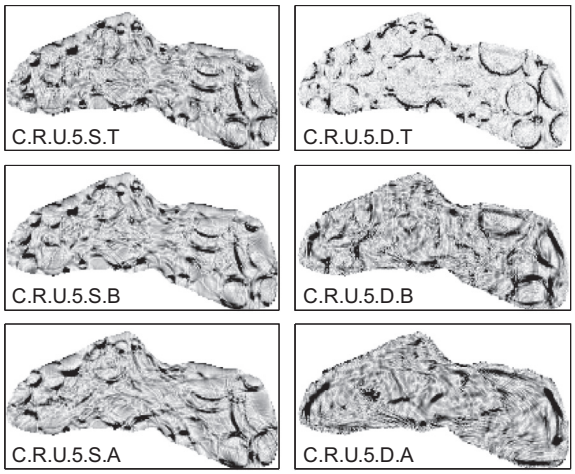

Fig. 3. Image reconstructions for model comet.

similarities in two images are perceived. Thus, the correlation term is supplemented by other factors. Wang et al. (2004) apply SSIM over a moving window to form a final MSSIM index; we neglected this step because we already had an optional AGC procedure.

SSIM applied directly to the migration-data images produced only a small improvement over r^2. However, robust results were obtained with SSIM on the analytic-signal envelopes. We also found the expected ordering of SSIM by assumed velocity model (True > Blurred > others). The remainder of our analysis exclusively treats SSIM of the analytic-signal envelopes, for the MaxNorm and the AGC-normalized analytic-signal amplitude. Note that SSIM of two positive quantities can be negative in exceptionally bad cases where the two factors are distributed bimodally close to each of their respective axes.

Because the distributions are strongly non-normal, we adopted the nonparametric Wilcoxon rank-sum test to assess differences by velocity model, normalization procedure, and the four parameters describing the experiment and the target. The p-value is the probability of observing a test statistic as or more extreme than the observed value under the null hypothesis that the distributions have equal medians. Applying the test pairwise to all of the results between two velocity models (for each normalization), we confirmed that the True medians were significantly higher than Blurred ($p < 0.01$), and in turn the Blurred medians were also significantly higher ($p < 0.01$) than each of the Average, Solid, and Regolith velocity models. However, there was no significant difference among these last 3 models ($p = 0.23$–0.88). We therefore treat only the True, Blurred, and Average velocity configurations hereafter.

Next, we compared the medians produced by the two normalizations for each of the three velocity models. We found that the MaxNorm median was significantly higher than the AGC ($p < 0.01$) for the Blurred and Average models, but the two were indistinguishable at the True model ($p = 0.63$). These results suggest exclusive use of SSIM-MaxNorm for further analysis, but it must be recognized that without the AGC, features closer to the surface are emphasized over those at depth.

Table 4 applies pairwise Wilcoxon rank-sum tests on the SSIM analytic-signal comparisons to the different values within each of the four main parameters (interior structure, attenuation level, radar frequency, and imaging geometry), for the various velocity models. Attenuation and Geometry are most frequently significant ($p \leqslant 0.05$), followed by Frequency, then Interior. Indeed, there is no statistical difference in the results obtained for the regolith vs. void interiors in any of the cases. The somewhat sharper qualitative assessment for the latter described above has no quantitative support. On the other hand, the median correlation statistics are improved by as much as 0.3–0.5 going from Single to Dual orbital geometry or from High to Low/Medium attenuation. The lower (5 MHz) frequency usually produced higher correlation compared to the higher (15 MHz) band, but at lower significance (see Figs. 4 and 5).

Statistics for the comet results are sparse because only six runs were executed. There is no significant difference

Table 4
Median statistics and Wilcoxon rank-sum p-values for 24 asteroid models.

Normalization	Velocity model	Interior (R, V)	Attenuation (H, M, L)	Frequency (5, 15)	Geometry (S, D)	Ranking ($p \leqslant 0.15$)
AGC	True, med. 0.38	Medians 0.40, 0.37 ($p = 0.98$)	0.17, 0.51, 0.68 (0.01,0.33)	0.36, 0.38 (0.93)	0.27, 0.78 (0.01)	Geom Atten
	Blurred, med. 0.21	0.21, 0.22 (0.66)	0.13, 0.24, 0.29 (0.06, 0.65)	0.25, 0.19 (0.10)	0.21, 0.26 (0.26)	Atten Freq
	Average, med. −0.04	−0.05, −0.03 (0.54)	−0.07, −0.04, 0.01 (0.11, 0.37)	−0.07, −0.03 (0.13)	−0.05, 0.01 (0.03)	Geom Atten/ Freq
Max Norm	True, med. 0.37	0.38, 0.36 (0.71)	0.27, 0.45, 0.75 (0.02, 0.28)	0.46, 0.37 (0.89)	0.30, 0.74 (0.03)	Atten Geom
	Blurred, med. 0.29	0.29, 0.31 (0.66)	0.27, 0.33, 0.31 (0.12, 0.88)	0.32, 0.28 (0.19)	0.28, 0.34 (0.08)	Geom Atten
	Average, med. 0.26	0.26, 0.25 (0.84)	0.21, 0.26, 0.27 (0.05, 0.49)	0.26, 0.25 (0.60)	0.25, 0.26 (0.62)	Atten

Correlations tested between SSIMs of image analytic-signal magnitudes.Unannotated numbers are medians; p-values for pairwise comparisons given in parentheses.
Strongest influences shaded ($p \leqslant 0.05$).

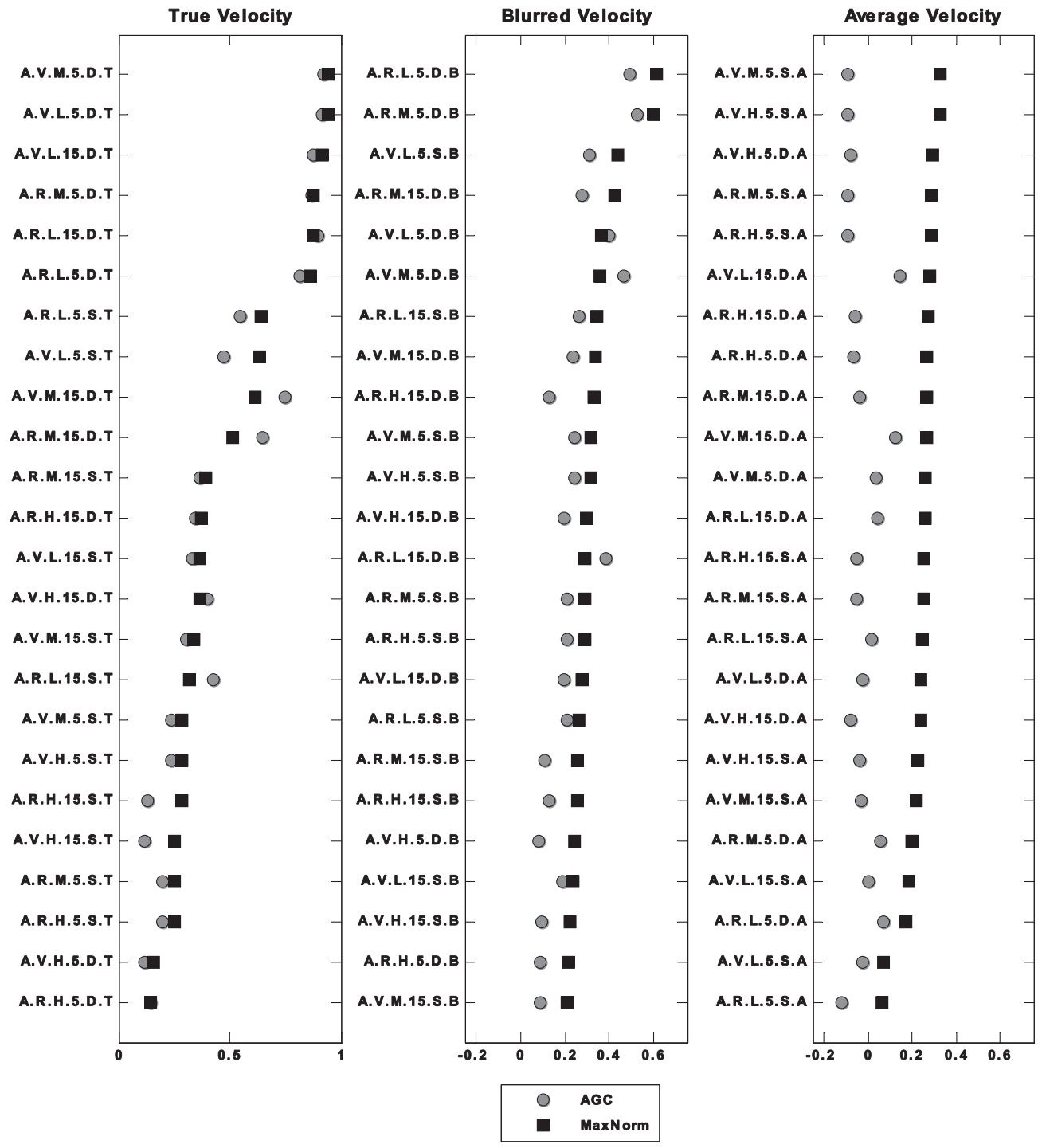

Fig. 4. Correlation of recovered images with Best image. Nomenclature follows Table 3. Image correlations are assessed by structural similarity index (SSIM) applied to the analytic-signal envelope of the reconstructed image. AGC applies 70-m moving window normalization to each image, whereas MaxNorm normalizes each image simply by its maximum value.

in the median SSIMs of these models and the median of the six most similar asteroid models ($p = 0.55$ for both MaxNorm and AGC). Quantitatively, imaging of the comet is not suffering appreciably from the double total attenuation compared to the asteroid. However, the standard deviation among the comet SSIMs is much smaller (0.05) than the comparable asteroid SSIMs (0.28): the hypothesis that the variances are the same can be rejected at $p = 0.004$. This indicates that the smaller velocity contrasts dampen the differences in the velocity models.

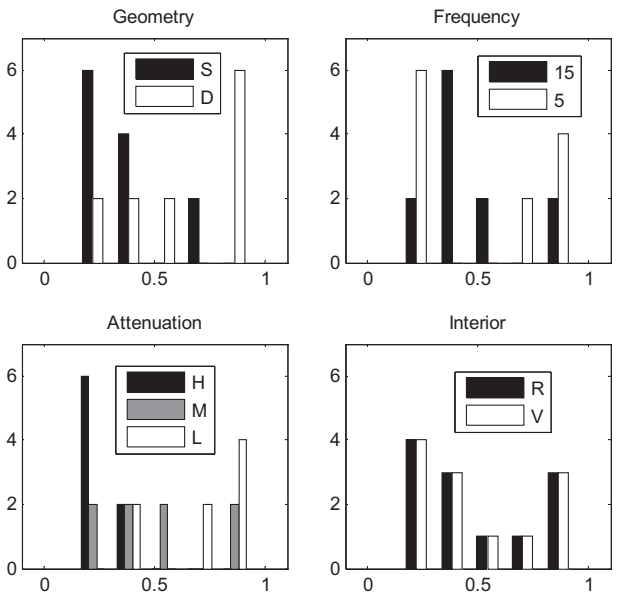

Fig. 5. Distribution of correlations (SSIM MaxNorm) for true velocity model. Improvements in correlation are significant ($p < 0.05$) between single and dual orbiter geometry and between high and medium/low target attenuation. There is minor improvement at 5 MHz vs 15 MHz but no differences if interior is regolith or void.

6. Concluding discussion

We performed migration imaging of radar wavefields modeled for asteroids and comets with different interior structures, attenuation rates, radar frequencies, observational geometries, and prior knowledge of the distribution of radar-wave velocities. We found that that the results did not depend strongly on target type (asteroid or comet) or interior structure (regolith vs void in block interstices) or frequency in the range 5–15 MHz. A major finding was that use of two spacecraft dramatically improves recovery of subsurface structure through diversity in viewing geometry and signal integration. Paper I describes this effect in more detail and with additional images. We also found that the velocity model had to be close to the true distribution in order to focus the echoes on the boundaries of the internal blocks. This limitation is much stronger for asteroid imaging than for often-cited analogues in medical imaging or even in most exploration seismology. However, the smaller velocity contrasts in comets mute both of these effects, allowing some imaging with an imperfect velocity model and with a single orbiter. Indeed, both the rubble-pile comet geometry and attenuative ice modeled here may be worst cases.

These findings suggest that both asteroids and comets are suitable targets for sounding: radar will fail to penetrate small asteroids only if attenuation lengths fall to tens of meters, which would apply to rocky objects as fractured as extensively as the terrestrial volcanic tuff selected here. Comets are easier targets, with their larger sizes largely offset by lower attenuation.

The Rosetta mission provides precedent for two spacecraft: in an alternative mission, the Philae lander could be modified to serve as an orbital receiver. The Apollo 15 and 16 subsatellites are also useful historical analogs, and the rapid growth in Earth-orbiting small satellites suggests the incremental cost of additional, redundant subsatellites may be tractable.

The choice for one or two spacecraft also controls how traveltime tomography will be performed: through-going rays would be used for two orbiters whereas surface echoes from the farside would be analyzed for a single orbiter. The reflected signal experiences some backscatter gain from the farside but it must pass through the object twice. Hence there is a maximum attenuation rate above which higher SNR is achieved by using two orbiters. Detailed analysis of SNR and velocity reconstruction for traveltime tomography using a suite of parameters comparable to that presented here will be the subject of a follow-on study. These considerations of migration and tomography will enable radar imaging of small bodies to elucidate their origin and evolution.

Acknowledgment

This work was supported by the NASA Planetary Instrument Definition and Development Program, Grant number NNX11AJ50G.

References

Asphaug and 11 others, 2003. Exploring asteroid interiors: the deep interior mission concept. In: Lunar Planet. Sci. Conf. XXXIV, Lunar Planet. Inst., Houston, #1906.

Asphaug and 23 others, 2010. Deep Interior radar imaging of comets. In: Lunar Planet. Sci. Conf. XVI, Lunar Planet. Inst., Houston, #2670.

Barriot, J.-P., Kofman, W., Herique, A., Leblanc, S., Portal, A., 1999. A two dimensional simulation of the CONSERT experiment (radio tomography of Comet Wirtanen). Adv. Space Res. 24, 1127–1138.

Benna, M., Barriot, J.P., Kofman, W., Barbin, Y., 2004. Generation of 3-D synthetic data for the modeling of the CONSERT experiment (the radiotomography of comet 67P/Churyumov–Gerasimenko). Antennas Propag. 52, 709–717.

Binzel, R.P. et al., 2003. Interiors of small bodies: foundations and perspectives. Planet. Space Sci. 51, 443–454.

Bondi, B., 2006. 3D Seismic imaging, Invest. Geophys. 14, Soc. Explor. Geophys. Tulsa.

Bottke, W.F., Cellino, A., Paolicchi, P., Binzel, R., 2002. An overview of the asteroids: the asteroids III perspective. In: Asteroids III. U. Arizona Press, pp. 3–15.

Britt, D.T., Yeomans, D., Housen, K., Consolmagno, G., 2002. Asteroid density, porosity, and structure. In: Bottke, W.F., Jr., Cellino, A., Paolicchi, P., Binzel, R.P. (Eds.), Asteroids III. University of Arizona Press, Tucson, pp. 485–500.

Brophy, J., 33 others, 2012. Asteroid retrieval feasibility study, Keck Inst. Space Studies, kiss.caltech.edu/study/asteroid/asteroid_final_report.pdf, 51 pp.

Carry, B., 2012. Density of asteroids. Planet. Space Sci. 73, 98–118.

Chan, V., Perlas, A., 2011. Basics of ultrasound imaging. In: Narouze, S.N. (Ed.), Atlas of Ultrasound-Guided Procedures in Interventional Pain Management. Springer, pp. 13–19.

Chapman, C.R., 2004. The hazard of near-Earth asteroid impacts on Earth. Earth Planet. Sci. Lett. 222, 1–15.

Chesley, S.R., 16 others, 2012. The trajectory dynamics of Near-Earth Asteroid 101955 (1999 RQ36), Asteroids Comets, and Meteors 2012, Lunar Planet Inst., #6470.

Claerbout, J., 1985. Imaging the Earth's Interior, Blackwell. Out-of-print; available online since 1996.

Daniels, D.J., 2004. Ground Penetrating Radar, 2nd ed. IEE, London.

Durda, D.D., Bottke Jr., W.F., Nesvorný, D., Enke, B.L., Merline, W.J., Asphaug, E., Richardson, D.C., 2007. Size-frequency distributions of fragments from SPH/*N*-body simulations of asteroid impacts: comparison with observed asteroid families. Icarus 186, 498–516.

Festou, M.C., Keller, H.U., Weaver, H.A., 2004. A brief conceptual history of cometary science. In: Festou, M.C., Keller, H.U., Weaver, H.A. (Eds.), Comets II. University of Arizona Press, Tucson, 745 pp.

Gaskell, R.W., 2008. Eros Shape Model V1.0, http://sbn.psi.edu/pds/resource/erosshape.html, NASA Planetary Data System.

Grimm, R.E., Heggy, E., Clifford, S., Dinwiddie, C., Mcginnis, R., Farrell, D., 2006. Absorption and scattering in ground penetrating radar: analysis of the Bishop Tuff. J. Geophys. Res. 111 (6), E06S02.

Grimm, R.E., Stillman, D.E., Dec, S.F., Bullock, M., 2008. Low-frequency electrical properties of polycrystalline saline ice and salt hydrates. J. Phys. Chem. 112, 15382.

Heggy, E. et al., 2007. Dielectric properties of chondrites and their implication in radar sounding of asteroid interiors. Lunar Planet. Sci. XXXVII, 1596.

Hilton, J.L., 2002. Asteroid masses and densities. In: Bottke, W.F., Jr., Cellino, A., Paolicchi, P., Binzel, R.P. (Eds.), Asteroids III. University of Arizona Press, Tucson, pp. 103–112.

Huebner, W.F., Greenberg, J.M., 2001. Methods for determining material strengths and bulk properties of NEOs. Adv. Space Res. 28, 1129–1137.

Kofman, W. et al., 2007. The comet nucleus sounding experiment by radiowave transmission (CONSERT): a short description of the instrument and of the commissioning stages. Space Sci. Rev. 128, 413–432.

Leinhardt, Z., Richardson, D.C., Quinn, T., 2000. Direct N-body simulations of rubble pile collisions. Icarus 146, 133–151.

Michel, P., Benz, W., Richardson, D.C., 2004. Catastrophic disruption of asteroids and family formation: a review of numerical simulations including both fragmentation and gravitational reaccumulations. Planet. Space Sci. 52, 1109–1117.

Nolan, M.C. et al., 2013. Shape model and surface properties of the OSIRIS-REx target asteroid (101955) Bennu from radar and lightcurve observations. Icarus 226, 629–640.

Olhoeft, G., Strangway, D., 1973. Dielectric properties of the first 100 meters of the Moon. Earth Planet. Sci. Lett. 24, 394–404.

Petrenko, V.F., Whitworth, R.W., 1999. Physics of Ice. Oxford Univ Press.

Picardi, G., et al., 2004. MARSIS: mars advanced radar for subsurface and ionosphere sounding. In: Mars Express – The Scientific Payload, ESA SP-1240, pp. 51–69.

Richardson, D.C., Leinhardt, Z.M., Melosh, H.J., Bottke Jr., W.F., Asphaug, E., 2002. Gravitational aggregates: evidence and evolution. In: Bottke, W.F., Jr., Cellino, A., Paolicchi, P., Binzel, R.P. (Eds.), Asteroids III. Univ. of Arizona Press, Tucson, pp. 501–515.

Safaeinili, A., et al., 2005. Deep interior mission: imaging the interior of near-earth asteroids using radio reflection tomography. In: Workshop Radar Investig., Lunar Planet Inst., Houston, #6017.

Safaeinili, A., Gulkis, S., Hofstadter, M.D., Jordan, R.L., 2002. Probing the interior of asteroids and comets using radio reflection tomography. Meteorit. Planet. Sci. 37, 1953–1963.

Sava, P., Ittharat, D., Grimm, R., Stillman, D., 2015. Radio reflection imaging of asteroid and comet interiors I: acquisition and imaging theory. Adv. Space Res. 55, 2149–2165.

Seu, R. et al., 2007. SHARAD sounding radar on the mars reconnaissance orbiter. J. Geophys. Res. 112. http://dx.doi.org/10.1029/2006JE002745.

Sheriff, R.E., Geldart, L.P., 1995. Exploration Seismology. Cambridge Univ. Press, New York, 592 pp.

Sihvola, A., 1999. Electromagnetic Mixing Formulas and Applications. IEE, London, 284 pp.

Stillman, D.E., Grimm, R.E., 2011. Radar penetrates only the youngest geological units on Mars. J. Geophys. Res. 116. http://dx.doi.org/10.1029/2010JE003661.

Stillman, D.E., Grimm, R.E., Dec, S.F., 2010. Low-frequency electrical properties of ice-silicate mixtures. J. Phys. Chem. B 114, 6065–6073.

Stuart, J.S., Binzel, R.P., 2004. Bias-corrected population, size distribution, and impact hazard for near-Earth objects. Icarus 170, 295–311.

Tanga, P., Cellino, A., Michel, P., Zappala, V., 1999. On the size distribution of asteroid families: the role of geometry. Icarus 141, 65–78.

Trudinger, C.M. et al., 1997. Modeling air movement and bubble trapping in firn. J. Geophys. Res. 102, 6747–6763.

Walker, J.D., Sagebiel, E.J., Huebner, W.F., 2006. A preliminary analysis of seismological techniques to study Eros and other asteroids. Adv. Space Res. 37, 142–152.

Wang, Z., Bovik, A.C., Sheikh, H.R., Simoncelli, E.P., 2004. Image quality assessment: from error visibility to structural similarity. IEEE Trans. Image Proc. 13, 600–612.

Weissman, P.R., Asphaug, E., Lowry, S.C., 2004. Structure and density of cometary nuclei. In: Festou, M.C., Keller, H.U., Weaver, H.A. (Eds.), Comets II. University of Arizona Press, Tucson, pp. 337–357, 745 pp.

Werner, S.C., Harris, A.W., Neukum, G., Ivanov, B.A., 2002. The near-earth asteroid size-frequency distribution: a snapshot of the lunar impactor size-frequency distribution. Icarus 156, 287–290.

Yilmaz, O., 2001. Seismic data analysis: society of exploration geophysicists, Tulsa.